Research Paper

Degradable Hollow Mesoporous Silicon/Carbon Nanoparticles for Photoacoustic Imaging-Guided Highly Effective Chemo-Thermal Tumor Therapy *in Vitro* and *in Vivo*

Jinfeng Zhang[1]*, Jun Zhang[3, 4]*, Wenyue Li[2, 4], Rui Chen[1], Zhenyu Zhang[2], Wenjun Zhang[2], Yongbing Tang[5], Xiaoyuan Chen[6], Gang Liu[3✉], Chun-Sing Lee[1✉]

1. Center of Super-Diamond and Advanced Films (COSDAF) & Department of Chemistry, City University of Hong Kong, 83 Tat Chee Avenue, Kowloon, Hong Kong SAR, P. R. China;
2. Center of Super-Diamond and Advanced Films (COSDAF) & Department of Physics and Materials Science, City University of Hong Kong, 83 Tat Chee Avenue, Kowloon, Hong Kong SAR, P. R. China;
3. State Key Laboratory of Molecular Vaccinology and Molecular Diagnostics Center for Molecular Imaging and Translational Medicine, School of Public Health, Xiamen University, Xiamen 361005, P. R. China;
4. Department of Ultrasound, Xijing Hospital, Xi'an, Shaanxi 710032, P. R. China;
5. Functional Thin Films Research Center, Shenzhen Institutes of Advanced Technology, Chinese Academy of Sciences;
6. Laboratory of Molecular Imaging and Nanomedicine (LOMIN), National Institute of Biomedical Imaging and Bioengineering (NIBIB), National Institutes of Health (NIH), MD 20892, USA.

* These authors contributed equally to this work.

✉ Corresponding authors: apcslee@cityu.edu.hk (C. S. Lee), gangliu.cmitm@xmu.edu.cn (G. Liu)

Abstract

The development of nanoscaled theranostic agents for cancer combination therapies has received intensive attention in recent years. In this report, a degradable hollow mesoporous PEG-Si/C-DOX NP is designed and fabricated for pH-responsive, photoacoustic imaging-guided highly effective chemo-thermal combination therapy. The intrinsic hollow mesoporous structure endows the as-synthesized nanoparticles (NPs) with a high drug loading capacity (31.1%). Under NIR (808 nm) irradiation, the photothermal conversion efficiency of the Si/C NPs is as high as 40.7%. Preferential accumulation of the PEG-Si/C-DOX NPs around tumor tissue was demonstrated with photoacoustic images. Cellular internalization of the NPs and release of the DOX in nuclei are shown with fluorescent images. With efficient NIR photothermal conversion and high DOX loading capacity, the PEG-Si/C-DOX NPs are demonstrated to have remarkable cancer-cell-killing ability and to achieve complete in vivo tumor elimination via combinational chemo-thermal therapy. Last but not least, the NPs show good biodegradability and biosafety, making them a promising candidate for multifunctional drug delivery and cancer theranostic.

Key words: degradable, silicon/carbon nanoparticles, photoacoustic imaging, chemo-thermal therapy.

Introduction

Over the past several decades, multifunctional nanoplatforms that combine diagnostic and therapeutic moieties for highly efficient antitumor treatments with low system toxicity have demonstrated encouraging promises in the fight against cancer [1-4]. In particular, combining photoacoustic imaging (PAI) with spatially precise photothermal therapy (PTT) has attracted much recent interests due to its high selectivity, deep penetration, non-invasiveness and good biosafety [5-10]. PAI as a new imaging modality shows distinct advantages over traditional optical imaging

techniques including higher spatial resolution and deeper tissue penetration, because it detects phonon which is scattered much less than photon in tissues.[11-14] PTT, which typically absorbs near-infrared (NIR) light (700-1300 nm) to generate heat for ablation of cancer cells. It has been considered as a promising modality for cancer treatment owing to its non-invasiveness and high selectivity without systemic side effects [15-17]. Furthermore, most PTT agents also enable PAI which endows the systems with additional diagnostic capabilities including locating the tumor site and monitoring PTT agents accumulation and their therapeutic responses [18-20]. However, complete elimination of tumor by a single PTT remains challenging because of absorption and scattering of light in biological tissues.[21] Thus, the combination of PTT with chemotherapy which could be delivered by a single nanoplatform has attracted extensive attention in recent years since it can minimize side effects, suppress drug resistance, and greatly improve therapeutic performance [8, 21-24].

Up to now, a variety of inorganic/polymer nanoplatforms, such as Au nanostructures [25-27], sulfides [16, 23, 28-31], transition metal oxides [32, 33], selenides [21, 34], Pd nanostructures [35, 36] and conductive polymer nanoparticles (NPs) [37-42], have been extensively employed as both PTT agents and drug carriers. However, a potential concern is that these inorganic and polymer nanomaterials are typically non-biodegradable and have possible long-term biotoxicity, which significantly hindered their further clinical translations [6, 43-45]. Therefore, the development of biocompatible and biodegradable PTT agents for efficient combinational chemo-thermal therapy is highly desirable [7, 9, 19, 46].

Herein, we report the applications of degradable hollow mesoporous silicon/carbon (Si/C) NPs as a carrier for a chemotherapeutic drug doxorubicin (DOX). Free DOX possesses serious limitations such as undesired systemic toxicity due to the lack of tumor selectivity during chemotherapy. The enhanced permeability and retention (EPR) effect is one of the most important features and advantage of nanomedicine which can be used to achieve enhanced accumulation in a tumor site [1, 2]. Porous silicon nanostructures present a promising class of nanoplatform for multiple bioapplications attributed to its intrinsic large cavity for drug loading and biodegradability as well as biocompatibility [47-52]. On the other hand, carbon based nanomaterials often have NIR absorption, excellent biocompatibility and high photostability and have drawn considerable attention for PAI and PTT [5, 53-56]. By combining the two materials, the Si/C NPs were found to be a biodegradable efficient PTT agent showing good

photoacoustic (PA) signal. Further loading of DOX into the Si/C NPs endows the system with additional fluorescent signal and chemotherapeutic effect leading to a highly efficient dual-modal imaging guided combinational chemo-PTT agent.

Results and Discussion

Preparation and Characterization of Hollow Mesoporous NPs

In this work, we prepared the monodispersed poly(maleic anhydride-alt-1-octadecene)-polyethylene glycol (C_{18}PMH-PEG) coated hollow mesoporous Si/C NPs loaded with a chemotherapeutic drug DOX for imaging-guided thermo-chemotherapy (termed as PEG-Si/C-DOX NPs) (Scheme 1). The mesoporous Si/C nanospheres were prepared according to our previous work [57, 58]. Firstly, SiO_2 NPs were fabricated by hydrolyzing reaction of tetraethyl orthosilicate (TEOS) (Scheme 1a). Polyacrylonitrile (PAN) used as carbon source and 3-aminopropyltriethoxysilane (APTES) served as a coupling agent were simultaneously dissolved into the dispersion of SiO_2 NPs. APTES molecules can be readily grafted onto the SiO_2 NPs surface through the formation of Si-O-Si bonds. Thus the PAN molecules can be easily adhered to the NPs surface due to interaction between their nitrile groups and the amine groups from APTES. Next, the PAN coated SiO_2 NPs were preoxidized in air to develop a carbon precursor coating on the SiO_2 NPs. The NPs were subsequently annealed in a reducing atmosphere to achieve reduction of SiO_2 to form mesoporous hollow Si nanospheres coated with carbon shell obtained by carbonization of the carbon precursor coating. As determined with thermogravimetric analysis, weight ratio of Si, SiO_2 and C in the Si/C NPs are 58%, 10% and 32% respectively. Because the Si core is used for loading a chemotherapeutic drug and the C shell is applied as a PTT agent, so we used "Si/C NPs" to present the as-prepared NPs. Further acid treatment improved the hydrophilicity of the Si/C NPs by attaching carboxyl and hydroxyl groups to the carbon shell. Finally, after DOX loading (Si/C-DOX) and PEG modification, the obtained hollow mesoporous PEG-Si/C-DOX NPs were successfully designed to integrate pH stimuli responsive properties, high drug loading capacity, photoacoustic/fluorescence dual-modal-imaging ability, combinational photothermal and chemotherapeutic effect, as well as biodegradability. With these merits, the PEG-Si/C-DOX NPs can act as an efficient multifunctional nanoplatform for highly effective synergistic cancer therapy *in vitro* and *in vivo* (Scheme 1b).
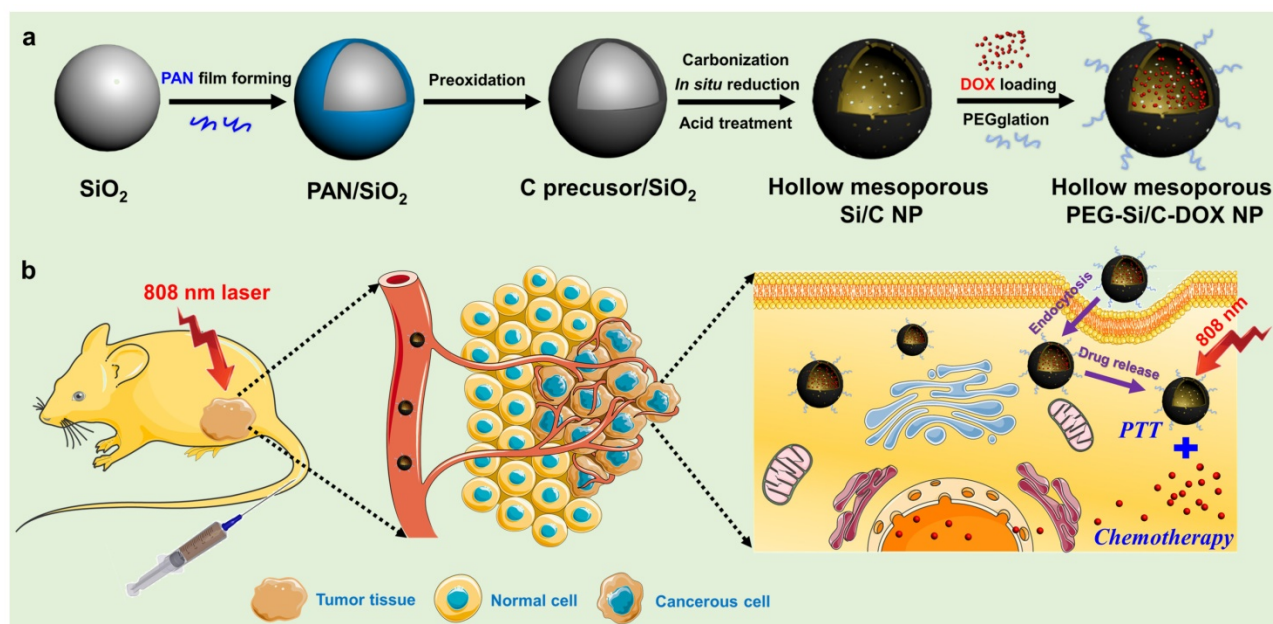
Scheme 1. a) Schematic illustration of fabrication of hollow mesoporous PEG-Si/C-DOX NP and b) its application for photoacoustic imaging-guided chemo-thermal therapy.

Representative scanning electron microscopic (SEM) and transmission electron microscopic (TEM) images of the as-prepared Si/C NPs are displayed in **Figure 1a and b**, showing their well-defined hollow nanospherical structure of about 200 nm in diameter. Corresponding elemental mappings on individual nanospheres (**Figure 1c–f**) further confirm the successful formation of inner cavity and element distribution in the Si/C NPs. It can be seen that outer shell of the NPs is composed of carbon originated from the PAN coating, while silicon distributes uniformly in inner shell of the NPs. A small amount of oxygen can be found in the shell because of incomplete reduction of SiO_2. Typical nitrogen adsorption/desorption isotherm technique further indicate the mesoporous structure of the as-fabricated Si/C NP which possesses high specific surface areas (67 m²/g), large pore volume (0.18 cm³/g) and very large average pore size (~10.7 nm) (**Figure 1g**). The specific surface area was determined with the BET method and the pore size distribution and pore volume were calculated with the Barrett-Joyner-Halenda (BJH) method. To further confirm the existence of small pores on the shell, HRTEM image was provided (**Figure S1**). The pores on the carbon shell can be clearly observed with the size of 5~15 nm, which is consistent with the BJH results. The large surface area and large pore size of the Si/C NPs are beneficial for getting high drug loading capacity, which is an important attribute for drug carriers. Hydrodynamic diameter distributions of the pristine, DOX-loaded and PEGylated Si/C NPs via DLS measurements are shown in **Figure 1h**. It can be

clearly found that the average diameter of the PEG-Si/C-DOX NPs (237 nm) is larger than that of the prestige Si/C NPs (211 nm) and the Si/C-DOX NPs (217 nm) by ~ 20 nm due to the PEG coating. On the other hand, size of the Si/C NPs shows much less changes upon drug loading as most drug molecules were accommodated within the pore channels and the hollow inner cavities. As presented in **Figure 1i**, the Si/C NPs have a negative surface charge of around -16.7 mV due to the attachments of carboxyl groups and hydroxyl groups during the acid treatment. This negative surface charge is beneficial for absorbing the DOX molecule which has a positive surface charge of 11.2 mV (**Figure 1i**). The reduced negative charge of Si/C-DOX NPs (-8.7 mV) demonstrates the successful absorption of DOX molecules into the Si/C NPs. Finally, the resulting PEG-Si/C-DOX NPs display a negative charge of around -11.8 mV after PEGylation. The PEGylation and negative charge could respectively prevent the nanocarriers from rapid clearance by the immune system and reduce the serum protein adsorption, thus prolonging blood circulation time of the PEGylated NPs and enhancing their accumulation at the tumor tissues [59].

The hollow mesoporous structure and the effective electrostatic interaction with drug molecules endow the as-synthesized Si/C NPs as an ideal carrier for loading anticancer drug DOX. To verify this, a Si/C NPs dispersion was impregnated with aromatic drug molecule DOX and then stirred for 48 h. After removal of excess unloaded free drug molecules by centrifugation, UV-vis spectra were measured to calculate drug loading content and drug

encapsulation efficiency on the Si/C NPs according to the standard absorbance curve of DOX (**Figure S2**). Weight ratios between the Si/C NPs and DOX were adjusted to obtain the optimal balance between the drug loading content (31.1 %) and drug encapsulation efficiency (56.5 %), as shown in **Table S1**. We select the weight ratio 5:4 here because both drug loading and encapsulation efficiencies resulted are high. However, when the weight of DOX fed initially at a very high concentration, the drug encapsulation efficiency would be decreased because the weight of DOX in the NPs almost reached a saturation condition. The high loading capacity of DOX in the Si/C NPs is probably due to (1) the above mentioned electrostatic interaction between DOX and silicon; (2) the mesoporous and hollow structures of the NPs and (3) π-π stacking interaction between DOX and carbon surface.[60] **Figure 1j** displays representative photographs of the free DOX solution, the Si/C NPs, the Si/C-DOX NPs and the PEG-Si/C-DOX NPs

dispersions respectively, indicating their good water dispersibility. To further show the incorporation of DOX, both UV-vis-NIR and fluorescence spectra of the free DOX, the Si/C NPs, the Si/C-DOX NPs and the PEG-Si/C-DOX NPs were respectively measured. As depicted in **Figure 1 k and l**, both UV-vis-NIR and fluorescence spectra of DOX-loaded NPs show the characteristic peaks of free DOX after drug loading, indicating that DOX molecules were absorbed into the NPs. Moreover, the DOX releasing from the PEG-Si/C-DOX NPs exhibits sustained pH-responsive release profiles (**Figure 1m**). At lower pH (5.0 and 6.2), protonation of the amine group on the DOX molecule (shown in **Figure S3**) will increase its hydrophilicity and solubility and weaken its interaction with the drug carrier surface.[61-63] This accelerates release of the drug molecules in more acidic tumor microenvironments and is in favor of minimizing the side effects of chemotherapeutics and enhancing the antitumor efficiency.
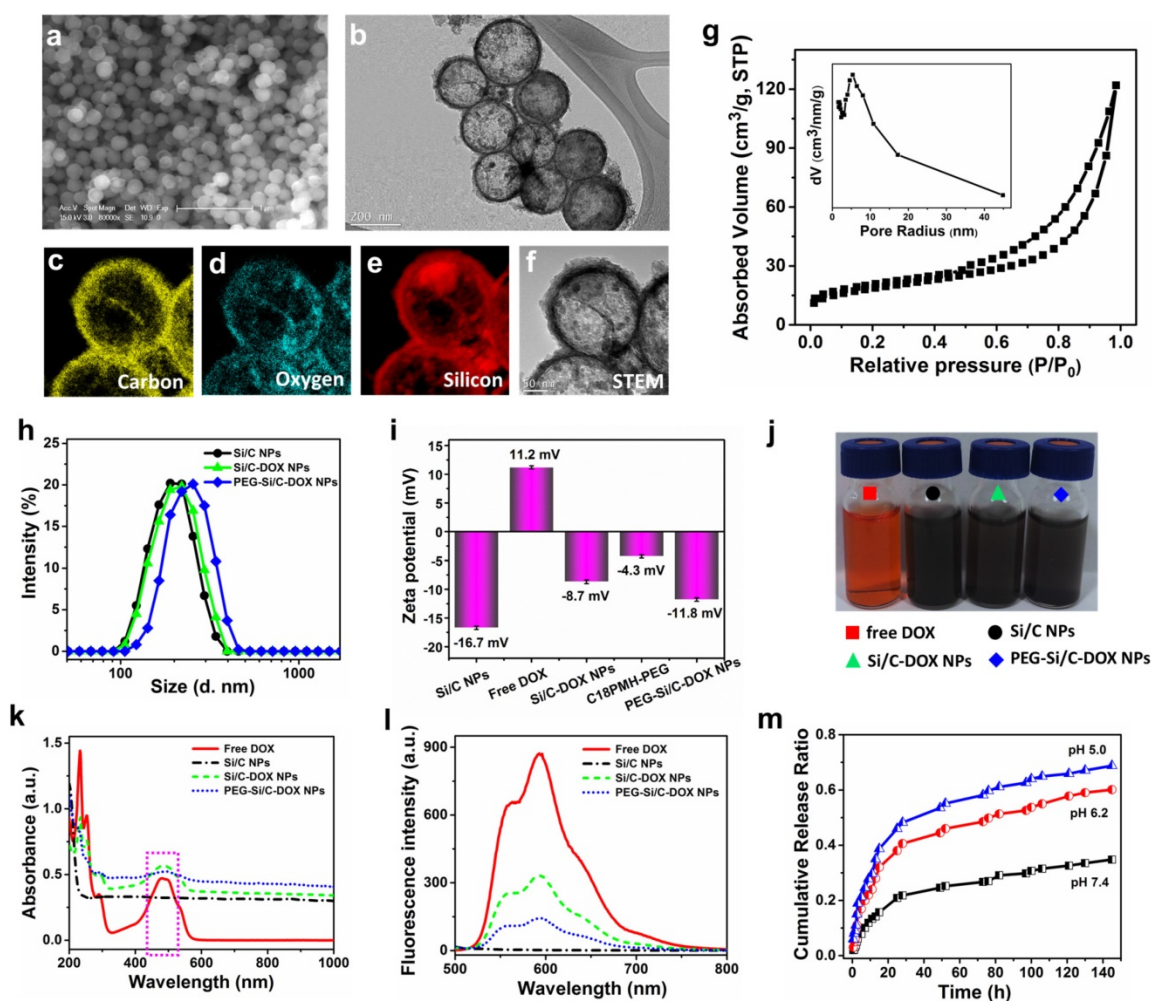

Figure 1. a) SEM and b) TEM images of the as-prepared Si/C NPs. Corresponding elemental mappings of the Si/C NPs c) carbon, d) oxygen, e) silicon, and f) scanning transmission electron microscopic (STEM) image; g) Nitrogen adsorption/desorption isotherms and the corresponding pore-size distribution curve (inset) of the Si/C NPs; h) Dynamic light scattering (DLS) measurements (Si/C: 211 nm; Si/C-DOX: 217 nm; PEG-Si/C-DOX: 237 nm) and i) zeta potential of the different NPs in DI water; j) representative photographs of free DOX (red), the Si/C NPs (black), the Si/C-DOX NPs (green) and the PEG-Si/C-DOX NPs (blue) solutions; k) UV-vis-NIR absorption and l) fluorescence spectra of free DOX, the Si/C NPs, the Si/C-DOX NPs and the PEG-Si/C-DOX NPs; m) The pH-dependent release of DOX from the PEG-Si/C-DOX NPs, which were cultured in buffer solutions of different pH values (pH 7.4, 6.2 or 5) with continuous shaking at 37 °C.

Photothermal and Photoacoustic Properties of the Si/C NPs

The UV-vis-NIR absorption spectra in Figure 1k show that the Si/C NPs, the Si/C-DOX NPs and the PEG-Si/C-DOX NPs possess strong absorption at the range of 700-1000 nm, while free DOX exhibits no obvious absorption beyond 700 nm, indicating that the characteristic NIR absorbance originates from Si/C NPs. To show the photothermal effects, photothermal heating curves of water, the free DOX, the PEG-Si/C NPs and the PEG-Si/C-DOX NPs were respectively measured under 1 W/cm² 808 nm laser irradiation for 10 min (Figure 2a). Both the PEG-Si/C NPs and the PEG-Si/C-DOX NPs exhibit remarkable temperature elevations reaching almost 70 °C, while the temperature variations for water and free DOX under the same irradiation dose are negligible. It is worth noting that this temperature enhancement is strongly concentration-dependent which facilitates the application of PEG-Si/C-DOX NPs as a photothermal agent by simplify adjusting the concentration to control temperature variation (Figure 2b). Furthermore, to evaluate the photothermal property of the Si/C NPs, the temperature variation of the solution was monitored as a function of time upon irradiation of an 808 nm laser (2 W/cm²). The NIR laser was turned off when the solution reached a steady-state temperature after irradiation for 490 s (Figure 2c). Based on reported method,[5] and the obtained data (Figure 2d), the photothermal conversion efficiency of the Si/C NPs was determined to be approximately 40.7%, which is much higher than those of commercial Au nanoshells (13%) and nanorods (21%),[64] $Cu_{2-x}S$ nanocrystals (16.3%),[65] $Cu_{2-x}Se$ (22%),[64] and MoS_2 nanosheets (24.4%).[28]
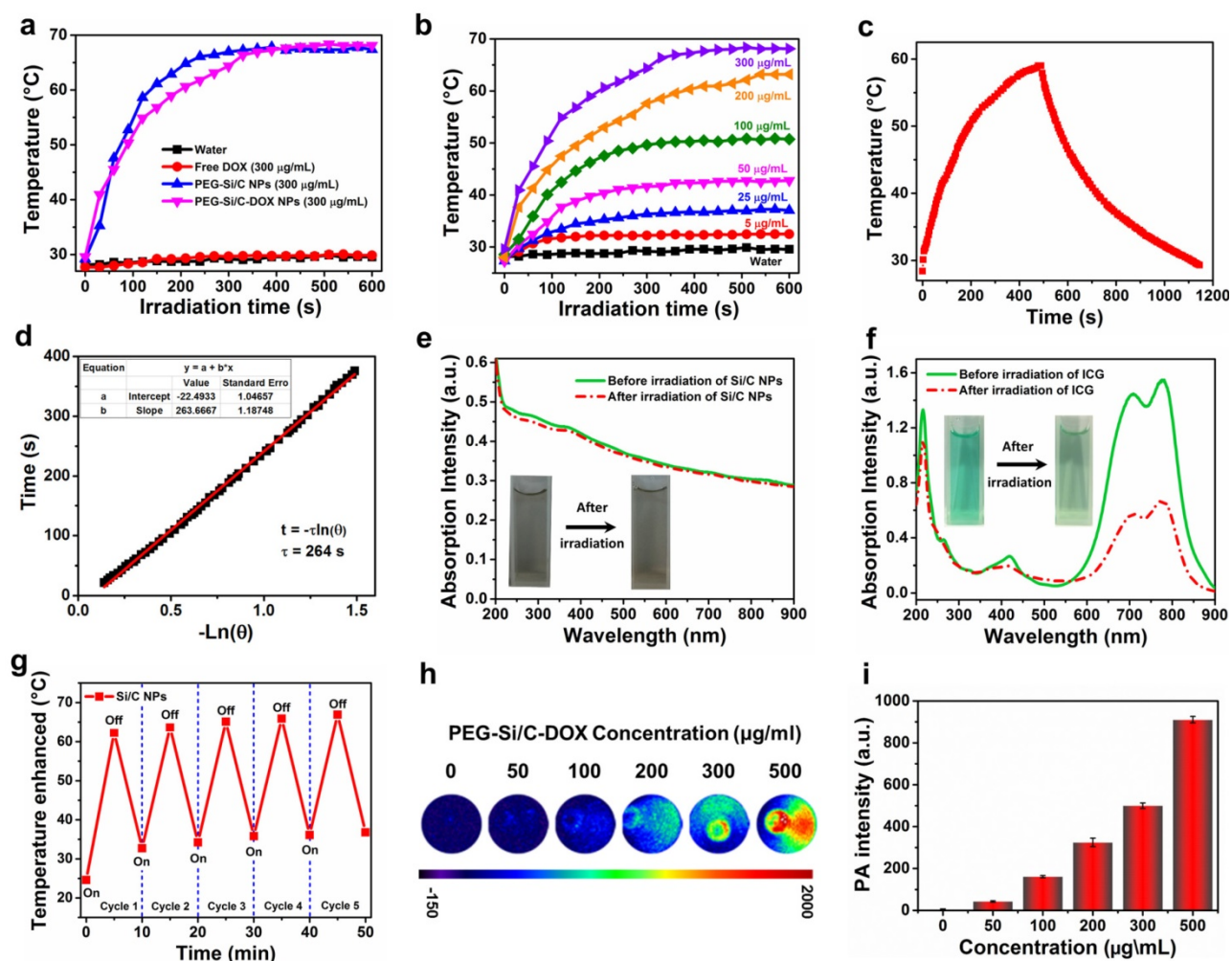

Figure 2. Photothermal and photoacoustic properties. a) Photothermal heating curves of water, free DOX, PEG-Si/C NPs and PEG-Si/C-DOX NPs upon 1 W/cm² 808 nm laser irradiation for 10 min; b) Photothermal heating curves of the PEG-Si/C-DOX NPs with different concentrations upon 1 W/cm² 808 nm laser irradiation; c) Photothermal effect of the Si/C NPs solution (0.2 mg/mL) under irradiation of an 808 nm laser which was turned off after irradiation for 490 s; d) Plot of cooling time versus negative natural logarithm of the temperature driving force obtained from the cooling stage as shown in c) (the time constant for heat transfer $τ_s$ = 264 s); UV-vis-NIR absorbance spectra of e) the Si/C NPs and f) indocyanine green (ICG) solutions before and after 808 nm laser irradiation at a power density of 0.8 W/cm² for 5 min, the insets are photos of the Si/C NPs and the ICG solutions before (left) and after (right) laser irradiation (the concentrations of the Si/C NPs and ICG solutions are 0.05 mg/mL); g) Temperature variations of the Si/C NPs (0.2 mg/mL) under 808 nm laser irradiation at a power density of 0.8 W/cm² for five light on/off cycles (5 min of irradiation for each cycle); h) Photoacoustic images and i) photoacoustic signal intensity of PEG-Si/C-DOX NP dispersions of different concentrations (0, 50, 100, 200, 300, 500 μg/mL, 800 nm laser)

To further confirm the potential of the Si/C NPs to serve as an effective PTT agent, their photothermal stability was compared with that of indocyanine green (ICG) which is a FDA-approved commercial PTT agent [66]. As depicted in **Figure 2e and f**, there is negligible degradation in UV-vis-NIR absorbance of the Si/C NPs, while the absorbance of ICG is largely diminished after 808 nm laser irradiation (0.8 W/cm²) for 5 min. The Si/C NPs dispersion show no observable color change, while the color of the ICG solution faded obviously. Furthermore, after five cycles of heating and cooling, the photothermal effect of the Si/C NPs remained stable reaching a temperature as high as ~ 65 °C (**Figure 2g**). The prominent photothermal stability of as-prepared NPs is obviously preferred as an excellent photothermal agent for cancer therapy.

Apart from the excellent photothermal performances, broad NIR absorption of the Si/C NPs also makes them as effective contrast agents for PAI over a large spectroscopy region from 600 to 1000 nm. To investigate their PA properties, PA images and corresponding PA signal intensities of the PEG-Si/C-DOX NPs at different concentrations were acquired upon excitation at 800 nm (**Figure 2h and i**). Compared with the control group without the PEG-Si/C-DOX NPs (0 μg/mL), the NPs samples present a dramatic PA effect. Moreover, the PA signal was also observed to be linearly correlated with the NP concentration (R² = 0.99) from 50 to 500 μg/mL as shown in **Figure S4**. This linear relationship is greatly beneficial for their future quantitative imaging applications.

In Vitro Degradation Behavior of Si/C NPs

As mentioned, good biodegradability is of great significance for drug carriers because the degradable carriers can minimize harmful effects caused by carrier accumulation. To investigate biodegradability of the as-prepared Si/C NPs, we determined the amount of silicon release upon incubation in PBS. Two Si/C NP dispersions (1 mg/mL) in PBS were first prepared by ultrasonication. One of the dispersions was immediately centrifuged to remove the NPs. The other NP dispersion in PBS was continuously shaken at pH 7.4 and 37 °C for simulating the physiological environment [50]. After 30 days of shaking, the sample was also centrifuged. Weights of silicon released into the two supernatants were then measured with inductive coupled plasma atomic emission spectroscopy (ICP-AES) as shown in Figure 3. It was found that without the 30 days shaking, only 0.35 wt% of silicon was released into the PBS solution. After 30 days shaking, 8.4 wt% of silicon from the original NPs has been dissolved into the PBS solution. This confirms that the Si/C NP is indeed degradable in the simulated physiological environment. Furthermore, morphologies of the NPs before and after shaking in PBS were respectively observed with SEM and TEM (insets of Figure 3). Morphological changes including collapse and break can be clearly observed in the shaken sample confirm the degradation.
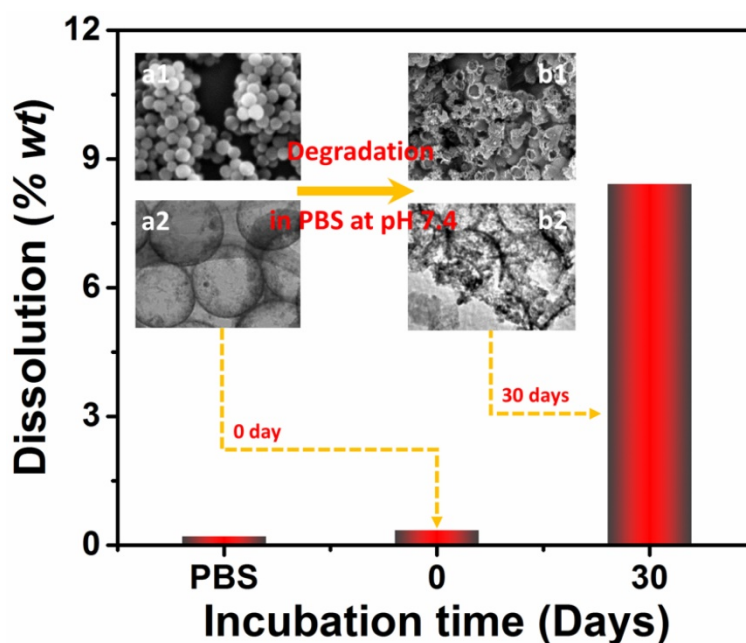

Figure 3. Weight percent of silicon dissolved in PBS without NPs and with Si/C NPs incubated in PBS for 0 day and 30 days at pH 7.4 with continuous shaking. The insets are respectively SEM (upper) and TEM (lower) images of the Si/C NPs before (a1, a2) and after (b1, b2) incubation in PBS for 30 days.
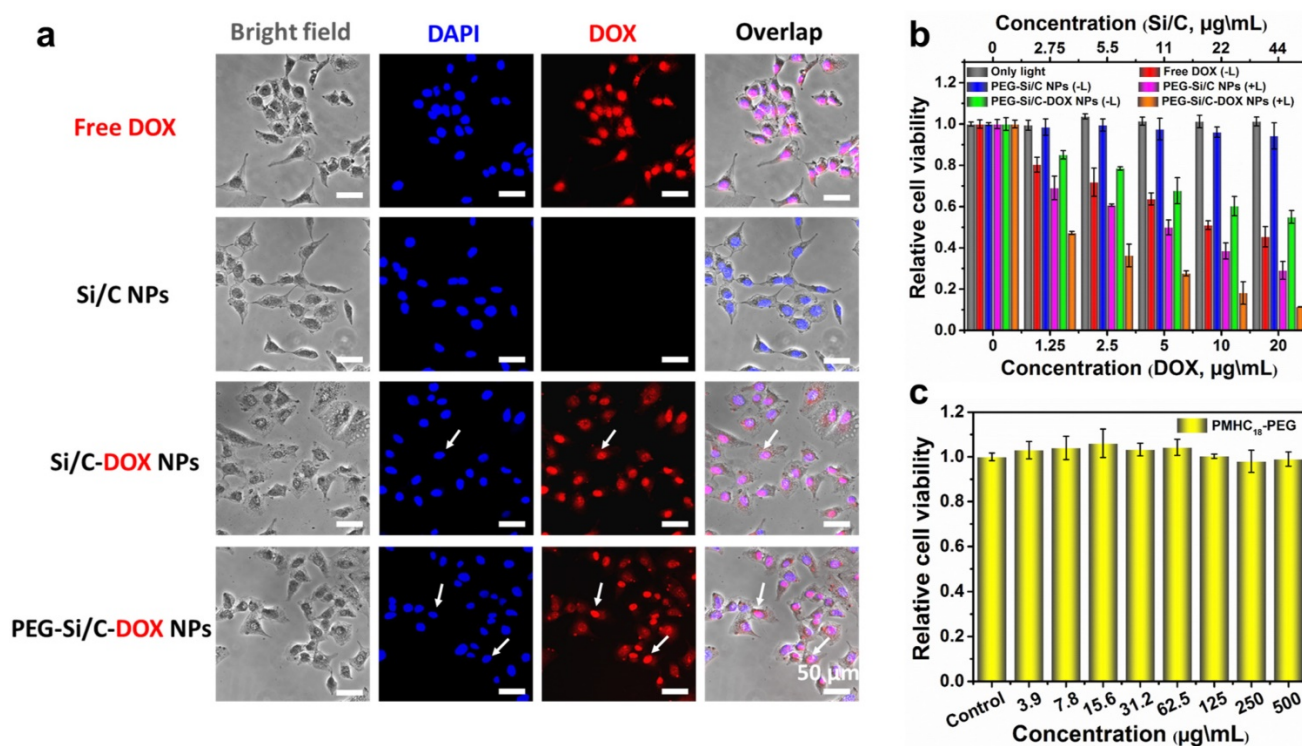
Figure 4. Cellular imaging and *in vitro* cytotoxicity. a) *In vitro* cellular imaging and localization of free DOX and different NPs, monitored in A549 cell; b) *In vitro* combination therapeutic effect of free DOX, the PEG-Si/C NPs, the PEG-Si/C-DOX NPs with or without 808 nm laser irradiation at a power density of 0.5 W/cm² for 5 min; c) *In vitro* cytotoxicity of the PMHC$_{18}$-PEG.

Cellular Fluorescence Imaging and *In Vitro* Cytotoxicity

We then investigated cellular internalization, fluorescent imaging and *in vitro* cytotoxicity of the PEG-Si/C-DOX NPs. First, fluorescent microscope was applied for cellular imaging and observing localization of the free DOX, the Si/C NPs, the Si/C-DOX NPs and the PEG-Si/C-DOX NPs in A549 cells at 37 °C for 4 hours. Fluorescence images were taken with 4, 6-diamidino-2-phenylindole (DAPI) as a nucleus-locating dye. As presented in **Figure 4a**, intense red fluorescence within nucleus can be clearly observed after cultured with both free DOX and the DOX-loaded NPs while no red signal detected in the Si/C NPs group, indicating the release and accumulation of DOX molecules within the cells. The white arrow shows that the released DOX molecules located in cell nucleus where DOX can induce cytotoxic activity by oxidative DNA damage. It is worth noting that the intensity of red signal from the free DOX in A549 cell is stronger than that of the NPs groups because of the different cellular uptake mechanism. Briefly, NPs are internalized into cells by endocytosis while the free DOX molecules penetrate cell and nuclear membranes through faster diffusion [67].

To evaluate *in vitro* combinational chemo-thermal therapeutic efficiency of the PEG-Si/C-DOX NPs, we measured the relative cell viability of treated A549 cell lines by using 3-(4,5-dimethylthiazol-2-yl)-2,5-diphenyltetrazolium bromide (MTT) assay. A549 cells were individually incubated with the free DOX, the PEG-Si/C NPs (with or without 808 nm laser irradiation), and the PEG-Si/C-DOX NPs (with or without 808 nm laser irradiation) for 24 hours. The control group is the cells with only laser irradiation but without any NPs. As depicted in **Figure 4b**, the free DOX, the PEG-Si/C NPs with irradiation, the PEG-Si/C-DOX NPs with or without irradiation show dose-dependent cytotoxicity while both the irradiation control group and the PEG-Si/C NPs without irradiation group exhibit negligible toxicity. These results suggest that the laser irradiation itself shows no cytotoxicity and that the PEG-Si/C NPs show excellent biocompatibility. Additionally, significantly enhanced cytotoxicity from a combination of chemotherapy and PTT was also observed. A549 cells exhibit the lowest cell viabilities upon laser irradiation in the presence of the PEG-Si/C-DOX NPs. In particular, along with the increase of NPs concentration (44 µg\mL, 20 µg\mL DOX-equivalent), a significant inhibition (up to 88.6%) of cell proliferation is observed, which is much more effective than individual conventional chemotherapy (free DOX) or PTT (the PEG-Si/C NPs with irradiation) alone. Next, to confirm that the

observed cytotoxicity is not caused by the PEGylation, we also carried out MTT assay for the C_{18}PMH-PEG surfactant as presented in **Figure 4c**, which shows that the surfactant has no cytotoxicity towards A549 cells even at a high concentration of 500 µg\mL. All these results suggest that the as-prepared PEG-Si/C-DOX NPs have a remarkable cell-killing ability, making it a promising nanoplatform for highly effective cancer combination therapy.

In Vivo Photoacoustic Images and Photothermal Effect at Tumor Sites

Besides evaluation on the photoacoustic and photothermal properties of the Si/C NPs *in vitro*, we also investigate their *in vivo* photoacoustic and photothermal effect at tumor site. As shown in Figure 5a, *in vivo* PA imaging of tumor tissue before and after tail intravenous injection of the PEG-Si/C-DOX NPs under 800 nm laser irradiation at different times (0.5, 1, 2, 4, 8 and 12 h) was conducted, inset is the corresponding normalized PA signals from the tumors at these time points. PA image of tumor without any treatment was recorded as control group

(0 h) showing only major blood vessels at the tumor sites in the absence of the NPs. After the injection, much stronger photoacoustic signals from the whole tumor can be detected, indicating the efficient accumulation of the PEG-Si/C-DOX NPs at the tumor sites owing to the EPR effect of tumors [1, 2].

Next, we evaluate the *in vivo* photothermal effect of the NPs at tumor sites. An infrared (IR) thermal camera was applied to take infrared images of the A549 tumor-bearing mice injected with PBS, the PEG-Si/C NPs and the PEG-Si/C-DOX NPs exposed to 808 nm laser at a power densities of 1 W/cm² at different time intervals (**Figure 5b**). Corresponding temperatures of the tumors after different irradiation times are shown in **Figure 5c**. As expected, both temperatures of tumors injected with the PEG-Si/C NPs and the PEG-Si/C-DOX NPs gradually increased from ~35 °C to ~50 °C within 10 min of laser irradiation. In comparison, tumors injected with only PBS under the same irradiation condition exhibited only a mild temperature increase and reached a plateau at ~38 °C.
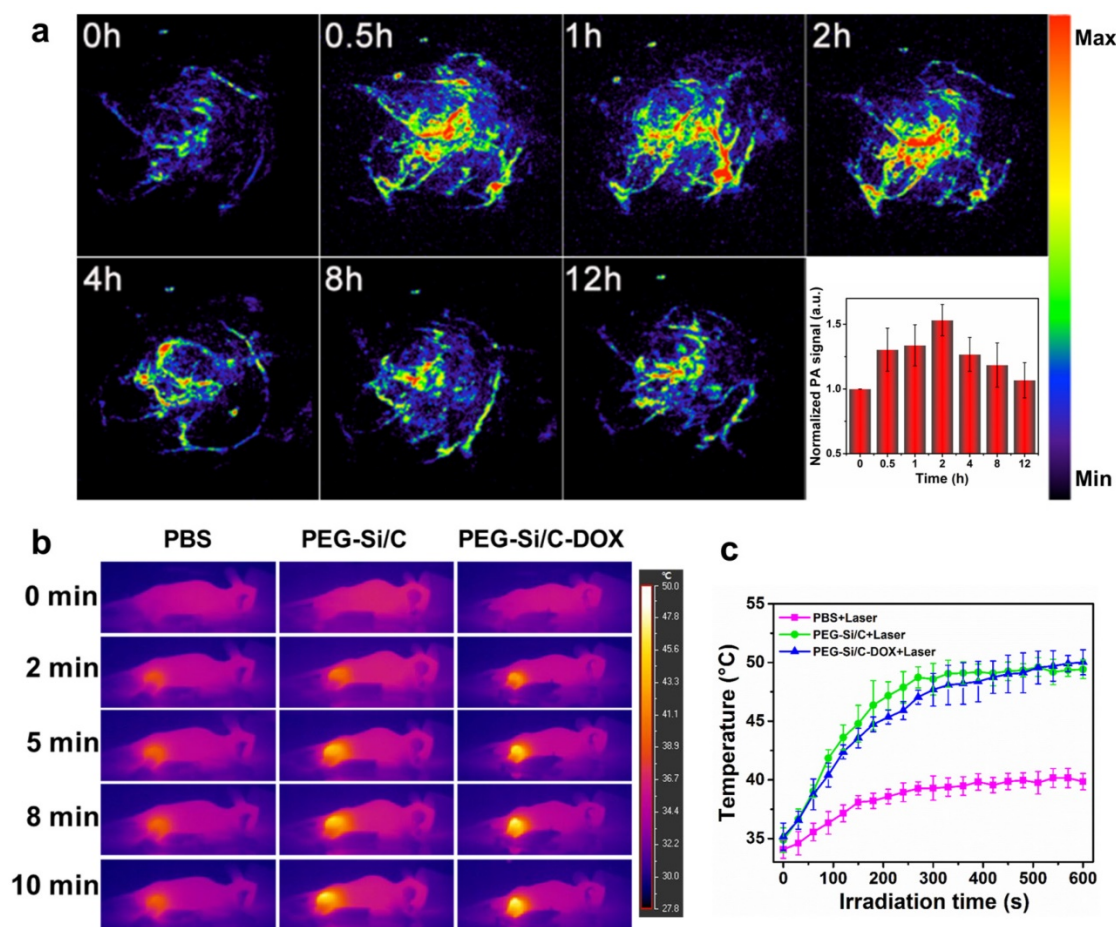

Figure 5. a) *In vivo* PA imaging of tumor tissue before and after tail intravenous injection of 250 µL PEG-Si/C-DOX NPs (2 mg/mL) under 800 nm laser irradiation at different time points (0.5, 1, 2, 4, 8 and 12 h), inset is the normalized PA signals in tumor at different time points; b) Infrared thermal images of A549 tumor-bearing mice injected with PBS, the PEG-Si/C NPs and the PEG-Si/C-DOX NPs exposed to 808 nm laser at a power densities of 1 W/cm² recorded at different time intervals, respectively; c) Temperature of tumors monitored by the infrared thermal camera in different groups upon laser irradiation as indicated in b).

In Vivo Antitumor Activity, Biodistribution and Biosafety

Encouraged by the impressive synergistic cell-killing ability *in vitro* and excellent photothermal performance *in vivo*, we subsequently carried out animal experiments to evidence the *in vivo* chemo-thermal tumor therapy using the PEG-Si/C-DOX NPs. The animal experimental strategy is illustrated in **Figure 6a**. 5×10^6 A549 cells were subcutaneously injected about two weeks before commencing treatment (black and gray boxes). When the tumors exhibited a volume of 80-100 mm^3, these mice were randomly divided into five groups with five mice in each cohort. The mice then received intravenous injections of various formulations (green boxes, Day 0) including PBS, PBS + Laser, free DOX, PEG-Si/C NPs + Laser, PEG-Si/C-DOX NPs + Laser, respectively (Laser irradiation: 808 nm, 1 W/cm^2 for 10 min). Both tumor volumes and mouse body weights were monitored every other day during the treatments. **Figure 6b** shows photographs of mice bearing A549 tumor after different treatments for varied time periods. It can be obviously seen that mice treatment with the combinational chemo-PTT (PEG-Si/C-DOX NPs with laser) shows the best effect on suppression the tumor (shown in red dotted circle) growth and achieve complete tumor regression. Comparing with the control group (PBS), treatment with PBS with laser irradiation shows little effect. Although mono-modal treatments with respectively chemotherapy (free DOX) and PTT (PEG-Si/C with laser) do slow down the tumor growth, their therapeutic efficacies are much lower than that of the combinational chemo-PTT treatment. Relative volumes of the tumors are also plotted in **Figure 6c**. This confirms observation from **Figure 6b** that the combinational chemo-PTT exhibits 100% tumor reduction while the mice in other four groups showed no or less tumor growth inhibition. Furthermore, as shown in **Figure 6d**, compared with the PBS group, no obvious weight loss was found in the tumor-bearing mice treated with PBS + Laser, PEG-Si/C NPs + Laser and PEG-Si/C-DOX NPs + Laser groups, indicating negligible side effect from the NPs nor laser irradiation. On the other hand, it should be pointed out that the free DOX group exhibits observable weight loss probably due to their lack of selectivity on killing both cancer and healthy cells [68].
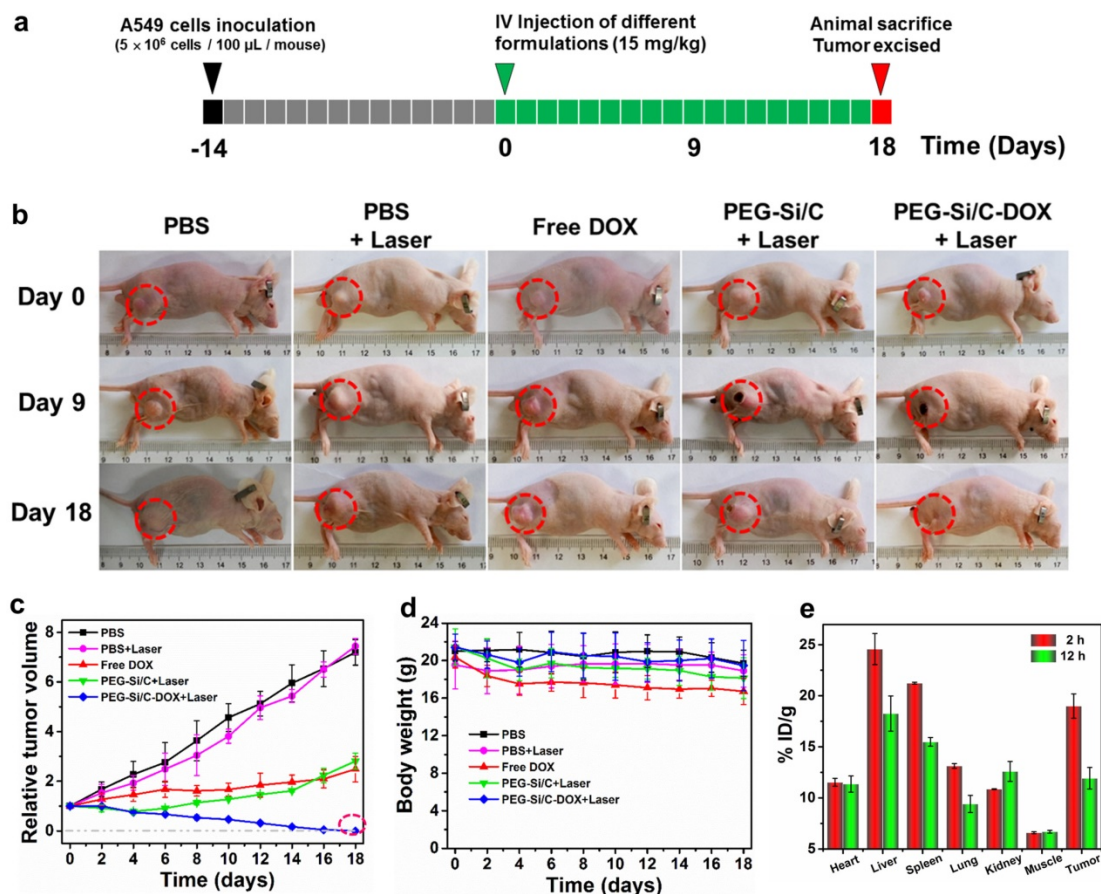

Figure 6. *In vivo* therapeutic efficacy of the PEG-Si/C-DOX NPs. b) Representative photographs of mice bearing A549 tumor after different treatments for varied time periods; c) Relative tumor volumes and d) body weight of mice treated with PBS, PBS + Laser, free DOX, PEG-Si/C NPs + Laser, PEG-Si/C-DOX NPs + Laser; e) Biodistribution of PEG-Si/C-DOX NPs via ICP-AES analysis of the silicon element at different times post-injection.
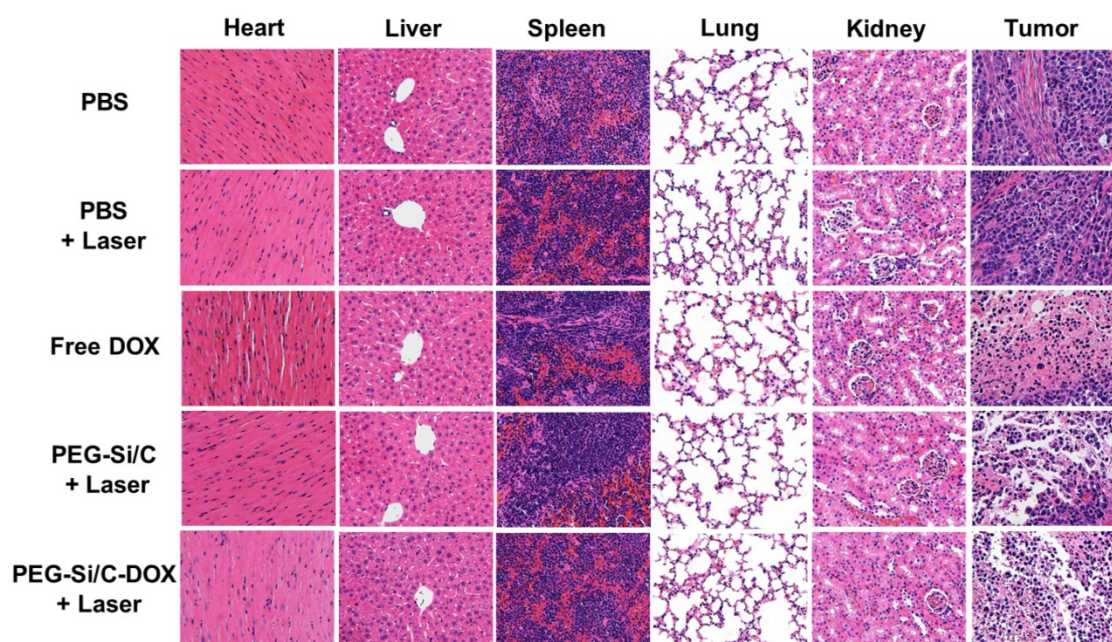
Figure 7. H&E staining images of major organs and tumor slices collected from mice post various treatments indicated.

To investigate the *in vivo* biodistribution of the PEG-Si/C-DOX NPs, quantitative measurements of tumor tissue and different major organs (heart, liver, spleen, lung and kidney) were obtained at 2 and 12 hours post-injection respectively via ICP-AES analysis of the silicon element. The silicon levels were shown in the unit of the percentage of injected dose per gram tissue (%ID/g). As exhibited in **Figure 6e**, the injected PEG-Si/C-DOX NPs are mainly distributed in the reticuloendothelial systems such as liver and spleen, which is widely observed for most nanomaterials, reflecting that the NPs are mainly eliminated by macrophage cells of the liver and spleen. Nevertheless, the accumulation level of the NPs in tumor is as high as ~ 19 % ID/g at 2 h post-injection owing to the effective EPR effect. The high accumulation of the NPs at tumor tissue is of great significance to achieve highly effective chemo-thermal tumor therapy.

In vivo biosafety has always been an important concern in the development of nanomaterials for their biomedical applications. Apart from measuring body weights of mice in each group (**Figure 6d**), we also collected the hematoxylin and eosin (H&E)-stained images of major organs (heart, liver, spleen, lung and kidney) and tumor histologic section from A549 tumor bearing mice in groups with different treatments (**Figure 7**). Compared to the control PBS group, there is no noticeable organ damage or inflammation lesion can be found in the laser or the NPs treated groups, suggesting no obvious organic dysfunction of mice induced by the applied laser or the PEG-Si/C-DOX NPs with irradiation treatment. In

addition, the H&E staining images of tumor sections further proved the remarkable chemo-thermal therapeutic effect of the PEG-Si/C-DOX NPs with laser irradiation. The nucleus presented in these images became smaller with shrinkage and the color of staining became shallower, indicating obvious cancer cell necrosis or apoptosis comparing to the PBS and only laser groups. Although the *in vivo* biosafety data shown here are preliminary, these results evidence that the PEG-Si/C-DOX NPs can serve as a potential non-toxic biodegradable nanomaterials for combinational tumor therapy.

Conclusions

In conclusion, we developed a degradable hollow mesoporous PEG-Si/C-DOX NPs for pH-responsive photoacoustic imaging-guided highly effective chemo-thermal combination therapy. The intrinsic hollow mesoporous structure and effective interactions including electrostatic attraction between DOX and silicon as well as the π-π stacking interaction between DOX and carbon surface endow the as-synthesized Si/C NPs as an ideal carrier for loading DOX with a high content (31.1%). Meanwhile, the PEG-Si/C-DOX NPs exhibits sustained pH-responsive release profile due to ready protonation of amine groups on DOX molecules at lower pH, which is greatly in favor of minimizing the side effects of chemotherapeutics and enhancing the antitumor efficiency. Moreover, the photothermal conversion efficiency of the Si/C NPs was determined to be as high as ~ 40.7%. Fluorescent images confirm the released DOX molecules can localize within

nucleus while photoacoustic images demonstrate the PEG-Si/C-DOX NPs can accumulate in tumor sites. Furthermore, combining strong NIR absorbance and high DOX loading capacity, the PEG-Si/C-DOX NPs can act as an excellent multifunctional nanoplatform for highly effective synergistic cancer therapy *in vitro* and *in vivo*. Not only the cytotoxicity experiments exhibit remarkable cell-killing ability but also the animal experiments show complete tumor elimination, suggesting the excellent therapeutic efficiency. Finally, the biodegradability of Si/C NPs and good biosafety make them a promising candidate for multifunctional drug delivery and tumor treatment, which will offer a new avenue for the future clinical application in the diagnosis and therapy of cancer.

Experimental Section

Materials

Tetraethyl orthosilicate (TEOS), polyacrylonitrile (PAN), dimethylformamide (DMF), 3-aminopropyltriethoxysilane (APTES), ammonia, ethanol, trimethylamine, doxorubicin (DOX), poly(maleicanhydride-alt-1-octa-decene) ($PMHC_{18}$), mPEG-NH_2 (5K), dichloromethane (DCM), 1-Ethyl-3-(3-dimethylaminopropyl)-carbodiimide (EDC), 3-(4,5-Dimethylthiazol-2-yl)-2,5-diphenyl tetrazolium bromide (MTT) were purchased from Sigma-Aldrich. Dulbecco's modified Eagle's medium (DMEM, high glucose), penicillin-streptomycin (10,000 U/mL), Dulbecco's phosphate buffered saline (PBS, 10X, pH 7.4), fetal bovine serum (FBS), and trypsin-EDTA (0.5%, no phenol red) were purchased from ThermoFisher Scientific.

Fabrication of the hollow mesoporous Si/C NPs and PEG-Si/C-DOX NPs

Firstly, SiO_2 NPs were fabricated from TEOS by hydrolyzing reaction. In brief, TEOS (6mL) was firstly injected into a mixture of ammonia (3 mL), deionized water (20 mL) and ethanol (140 mL). The mixture was then hydrolyzed for 3 hours under continuous stirring. The resulting solution was centrifuged and washed with Milli-Q water and ethanol respectively for three times. The SiO_2 NPs were acquired after drying at 100 °C. To obtain the hollow mesoporous Si/C NPs, as-fabricated SiO_2 NPs (0.3 g) was dispersed in DMF under sonication for 1 h. PAN used as carbon source (0.1 g) and APTES (a few drops) used as a coupling agent were respectively dissolved into the dispersion of SiO_2 NPs. Subsequently, the DMF was completely removed by evaporating at 140 °C under strong stirring. Next, the PAN coated SiO_2 NPs were preoxidized to get the carbon precursor coated

NPs upon annealing in a muffle furnace at 250 °C for 2 h. The sample was then homogeneously mixed with magnesium powder and loaded into a corundum boat. The as-obtained NPs were subsequently annealed at 800 °C for 3 h with a steady flow of 5% H_2 in Ar to achieve polymer carbonization and *in situ* SiO_2 to Si reduction. After cooling, the sample was stirred in a 2 M HCl solution for 2 h at room temperature to remove the magnesia. For the reduction of SiO_2, O atoms in SiO_2 diffuse outward and the Mg atoms diffuse inward due to the concentration gradients. Mg is oxidized into MgO and some of these MgO nanoparticles may imbedded into the shell during the PAN transforming into carbon. After this annealing treatment, HCl solution was used to remove the MgO which results in the formation of pores in the carbon shell.[69,70] Finally, the sample was filtered and washed with deionized water until pH ~ 7. The hollow nanospheres were finally obtained by drying under vacuum at 60 °C for 8 h. Afterwards, further acid treatment (nitric acid) improved the hydrophilicity of the as-prepared Si/C NPs by attaching carboxyl groups and hydroxyl groups to the surface.

To load the DOX into the mesoporous hollow Si/C NPs, a mixture of Si/C NPs (5 mg/mL) and DOX solution (4 mg/mL) was prepared in a 50 mL round-bottom flask and stirred at 37 °C for 48 h. Weight ratios between the Si/C NPs and DOX were adjusted to obtain the optimal balance between the drug loading content and drug encapsulation efficiency. Then the suspension was centrifuged at 14000 rpm for 30 min in propylene tubes and washed three times with Milli-Q water to remove the unloaded excess DOX. Finally the Si/C-DOX NPs were re-suspended in PBS and stored at 4 °C. The DOX drug loading content and drug encapsulation efficiency were determined via UV-vis absorbance spectroscopy measurements at 480 nm absorbance peak according to standard absorbance curve of DOX.

C_{18}PMH-PEG was synthesized by reacting C_{18}PMH with mPEG-NH_2. In brief, mixture of C_{18}PMH (10 mg) and mPEG-NH_2 (143 mg) were dissolved in DCM (5 mL), then triethylamine (6 μL) and EDC (10 mg) were respectively added in the above solution during their stirring. After 24 h, the DCM solvent was completely evaporated by blowing with dry N_2. The obtained sample was then dissolved in deionized water and dialyzed in deionized water for 3 days in a dialysis bag (the molecular weight cut-off is 14000 Da) to get rid of unreacted chemicals. After freeze-drying, the final white product was kept at 4 °C. For functionalization of the Si/C NPs or Si/C-DOX NPs, 500 μL of 3 mg/mL C_{18}PMH-PEG solution was added to Si/C NPs or Si/C-DOX NPs

suspensions (5 mL). The mixture was stirred for 30 min. After centrifugation and washing three times with PBS, C_{18}PMH-PEG would attach to the surface of the Si/C NPs or the Si/C-DOX NPs by non-covalent hydrophobic interaction. Finally the resulting PEG-Si/C NPs and PEG-Si/C-DOX NPs were respectively stored at 4 °C for future use.

The drug loading content (LC) and drug encapsulation efficiency (EE) were calculated according to the following equations: LC (wt %) = (weight of DOX in the NPs/weight of DOX loaded NPs) ×100%; EE (%) = (weight of DOX in the NPs /weight of DOX fed initially) × 100%.

Characterization of the as-prepared Si/C NPs

Size and morphology of the Si/C NPs were firstly investigated using SEM (Philips XL-30 FEG). The SEM samples were prepared by dropping a dispersion of the Si/C NPs on a Si substrate. TEM, element mappings and STEM were performed on a JEM-2100F electron microscope operated at 200 kV. The TEM samples were prepared by dripping Si/C NPs dispersion onto a carbon film followed by natural drying. DLS and zeta potential measurements were performed by using a Malvern Zetasizer instrument.

UV-vis/ UV-vis-NIR, Fluorescence and ICP-AES measurements

UV-vis spectra were obtained by using a Cary 50Conc UV-Visible Spectrophotometer while UV-vis-NIR spectra were measured using a PE Lamda 19 UV-vis-NIR Spectrophotometer. Fluorescence spectra were obtained by using a Cary Eclipse Fluorescence Spectrophotometer. ICP-AES analysis of the silicon element was obtained by a PE 2100DV inductively Coupled Plasma Atomic Emission Spectrometer.

In vitro pH-dependent drug-release

Firstly, PEG-Si/C-DOX NPs were cultured in buffer solutions of different pH values (pH 7.4, 6.2 or 5). The different pHs obtained by mixing buffer solutions of Na_2HPO_4 and citric acid in different ratios. Secondly, 5 mL of each suspension were added into a propylene tube followed by continuous shaking at 37 °C. Thirdly, at different time points, after centrifugation for 10 min, 2 mL of supernatant were collected from the solution. Then the solution volume was maintained constant by adding 2 mL of buffer solutions of given pH values. The amount of the released DOX was measured via UV-vis absorbance spectroscopy using the 480 nm absorbance peak of DOX.

In Vivo photoacoustic imaging

PA imaging was obtained by using an Endra Nexus 128 scanner (Ann Arbor, MI, USA). 1-2% isoflurane mixed with pure oxygen was used to maintain anesthesia of the mice during the whole experiments. The body temperature of the mice was maintained at 37.5 °C by using a water heating system during the scans. 800 nm were selected as the working laser wavelength. PA scans were performed before and after the injection of the PEG-Si/C-DOX NPs via mouse tail vein at 0.5, 1, 2, 4, 8 and 12 h post-injection.

In vitro uptake and fluorescence imaging

A549 cells were cultured with DMEM (Invitrogen) supplemented with 10 % FBS (Gibco) and 1% penicillin/streptomycin (Gibco) in 5% CO_2 at 37 °C in a standard incubator. The cells were trypsinized for 4 min and recultured on 60 mm culture dishes. In the next day, the cells were then trypsinized and seeded on 6-well plates. After incubation in an incubator at 37 °C with 5% CO_2 for 24 h. The free DOX, the Si/C NPs, the Si/C-DOX NPs and the PEG-Si/C-DOX NPs were respectively added to each well. The treated cells were then returned to the incubator for another 4 h. After that, the plates were washed three times with sterile PBS. DAPI was used to stain the cell nuclei for 5 min after fixing the treated cells. Finally, fluorescent imaging experiments were performed by using a Nikon ECLIPSE 80i fluorescent microscope.

In vitro cytotoxicity by MTT assay

The A549 cells were cultured on 96-well plates in DMEM supplemented with 10 % FBS (Gibco) and 1% penicillin/streptomycin (Gibco). After growing overnight, the cells were used for experiments. The original medium was removed totally in each well, then 200µl of DMEM containing given concentrations of free DOX, the PEG-Si/C NPs and the PEG-Si/C-DOX NPs were added to the 96-well plates. The final concentration of Si/C in each plate ranged from 2.75 to 44 µg\mL, the corresponding final concentration of DOX in each plate ranged from 1.25 to 20 µg\mL. After 12 h incubation in the dark at 37 °C, the cells incubated with the PEG-Si/C NPs and the PEG-Si/C-DOX NPs were irradiated with or without 808 nm laser at the power density of 0.5 W/cm² for 5 min. The plates were then incubated at 37 °C in the dark for another 12 h. The control group is the cells with only laser irradiation but without any NPs. Subsequently, removed the original medium and added a mixture of 180 µL of DMEM (without FBS) and 20 µL of MTT (Invitrogen) stock solution (5 mg/mL in sterile PBS) in each well. After incubation for 4 hours, the medium (containing MTT) was

removed completely, then adding DMSO (200 µL, Sigma-Aldrich) to each well. *In vitro* cell viabilities were measured by using a BioTek Powerwave XS microplate reader which to read the absorbance at 540 nm. The cells incubated with DMEM without any treatment represented 100% cell survival.

In Vivo antitumor activity, biodistribution and biosafety

5-6 weeks age of T-cell deficient male nude (nu/nu) mice were purchased from the Shanghai Slac Laboratory Animal Co. Ltd (Shanghai, China). 5×10^6 A549 cells were subcutaneously injected about two weeks before commencing treatment. When the tumors exhibited a volume of 80-100 mm³, these mice were randomly divided into five groups with five mice in each cohort. The mice then received intravenous injections of various formulations (Day 0) including PBS, PBS + Laser, free DOX, PEG-Si/C NPs + Laser, PEG-Si/C-DOX NPs + Laser, respectively (Laser irradiation applied: 808 nm, 1 W/cm² for 5 min; concentration of various formulations: 1 mg/mL, 300 µL). The final injected dose was 15 mg/kg/mouse. Both tumor volumes and mouse body weights were monitored every other day during the period of study (18 days). After 18 days from drugs administration, the mice were sacrificed. Both tumor tissue and major organs including heart, liver, spleen, lung, and kidney were dissected for H&E staining. The *in vivo* biodistribution of the PEG-Si/C-DOX NPs in A549 tumor bearing mice was determined via ICP-AES analysis of the silicon element.

Acknowledgment

Supplementary Material

Supplementary figures.
http://www.thno.org/v07p3007s1.pdf

Competing Interests

The authors have declared that no competing interest exists.

References

1. Ferrari M, Cancer nanotechnology: opportunities and challenges. Nat. Rev. Cancer 2005; 5: 161−171.
2. Davis ME, Chen G, Shin DM. Nanoparticle therapeutics: an emerging treatment modality for cancer. Nat. Rev. Drug Discov. 2008; 7: 771−782.
3. Cheng Z, Zaki AA, Hui JZ, Muzykantov VR, Tsourkas A. Multifunctional nanoparticles: cost versus benefit of adding targeting and imaging capabilities. Science 2012; 338: 903−910.
4. Li C. A targeted approach to cancer imaging and therapy. Nat. mat. 2014; 13: 110−115.
5. Ge J, Jia Q, Liu W, Guo L, Liu Q, Lan M, Zhang H, Meng X, Wang P. Red-emissive carbon dots for fluorescent, photoacoustic, and thermal theranostics in living mice. Adv. Mater. 2015; 27: 4169−4177.
6. He X, Bao X, Cao H, Zhang Z, Yin Q, Gu W, Chen L, Yu H, Li Y. Tumor-penetrating nanotherapeutics loading a near-infrared probe inhibit growth and metastasis of breast cancer. Adv. Funct. Mater. 2015; 25: 2831−2839.
7. Song G, Hao J, Liang C, Liu T, Gao M, Cheng L, Hu J, Liu Z. Degradable molybdenum oxide nanosheets with rapid clearance and efficient tumor homing capabilities as a therapeutic nanoplatform. Angew. Chem. Int. Ed. 2016; 55: 2122−2126.
8. Cai X, Jia X, Gao W, Zhang K, Ma M, Wang S, Zheng Y, Shi J, Chen H. A versatile nanotheranostic agent for efficient dual-mode imaging guided synergistic chemo-thermal tumor therapy. Adv. Funct. Mater. 2015; 25: 2520−2529.
9. Lee MY, Lee C, Jung HS, Jeon M, Kim KS, Yun SH, Kim C, Hahn SK. Biodegradable photonic melanoidin for theranostic applications. ACS Nano 2016; 10: 822−831.
10. Zeng J, Cheng M, Wang Y, Wen L, Chen L, Li Z, Wu Y, Gao M, Chai Z. pH-Responsive fe(iii)–gallic acid nanoparticles for in vivo photoacoustic imaging-guided photothermal therapy. Adv. Healthcare Mater. 2016; 5: 772−780.
11. Pu K, Shuhendler AJ, Jokerst JV, Mei J, Gambhir SS, Bao Z, Rao J. Semiconducting polymer nanoparticles as photoacoustic molecular imaging probes in living mice. Nat. Nanotechnol. 2014; 9: 233−239.
12. Zhang Y, Jeon M, Rich LJ, Hong H, Geng J, Zhang Y, Shi S, Barnhart TE, Alexandridis P, Huizinga JD, Seshadri M, Cai W, Kim C, Lovell JF. Non-invasive multimodal functional imaging of the intestine with frozen micellar naphthalocyanines. Nat. Nanotechnol. 2014; 9: 631−638.
13. An FF, Deng Z, Ye J, Zhang J, Yang YL, Li C, Zheng CJ, Zhang X. Aggregation-induced near-infrared absorption of squaraine dye in an albumin nanocomplex for photoacoustic tomography in vivo. ACS Appl. Mater. Interfaces 2014; 6: 17985−17992.
14. Miao Q, Lyu Y, Ding D, Pu K. Semiconducting oligomer nanoparticles as an activatable photoacoustic probe with amplified brightness for in vivo imaging of pH. Adv. Mater. 2016; 28: 3662−3668.
15. Lovell JF, Jin CS, Huynh E, Jin H, Kim C, Rubinstein JL, Chan WCW, Cao W, Wang LV, Zheng G. Porphysome nanovesicles generated by porphyrin bilayers for use as multimodal biophotonic contrast agents. Nat. Mater. 2011; 10: 324−332.
16. Li B, Ye K, Zhang Y, Qin J, Zou R, Xu K, Huang X, Xiao Z, Zhang W, Lu X, Hu J. Photothermal theragnosis synergistic therapy based on bimetal sulphide nanocrystals rather than nanocomposites. Adv. Mater. 2015; 27: 1339−1345.
17. Zhu X, Feng W, Chang J, Tan YW, Li J, Chen M, Sun Y, Li F. Temperature-feedback upconversion nanocomposite for accurate photothermal therapy at facile temperature. Nat. Commun. 2016; 7: 10437.
18. Kim JW, Galanzha EI, Shashkov EV, Moon HM, Zharov VP. Golden carbon nanotubes as multimodal photoacoustic and photothermal high-contrast molecular agents. Nat. Nanotechnol. 2009; 4: 688−694.
19. Liu J, Wang P, Zhang X, Wang L, Wang D, Gu Z, Tang J, Guo M, Cao M, Zhou H, Liu Y, Chen C. Rapid degradation and high renal clearance of Cu_3BiS_3 nanodots for efficient cancer diagnosis and photothermal therapy in vivo. ACS Nano, 2016; 10: 4587−4598.
20. Lyu Y, Fang Y, Miao Q, Zhen X, Ding D, Pu K. Intraparticle Molecular Orbital Engineering of Semiconducting polymer nanoparticles as amplified theranostics for in vivo photoacoustic imaging and photothermal therapy. ACS Nano 2016; 10: 4472−4481.
21. Li Z, Hu Y, Howard KA, Jiang T, Fan X, Miao Z, Sun Y, Besenbacher F, Yu M. Multifunctional bismuth selenide nanocomposites for antitumor thermo-chemotherapy and imaging. ACS Nano 2016; 10: 984−997.
22. Zhang Z, Wang J, Nie X, Wen T, Ji Y, Wu X, Zhao Y, Chen C. Near infrared laser-induced targeted cancer therapy using thermoresponsive polymer encapsulated gold nanorods. J. Am. Chem. Soc. 2014; 136: 7317−7326.
23. Wang S, Chen Y, Li X, Gao W, Zhang L, Liu J, Zheng Y, Chen H, Shi J. Injectable 2D MoS₂-integrated drug delivering implant for highly efficient NIR-triggered synergistic tumor hyperthermia. Adv. Mater. 2015; 27: 7117−7122.

24. Zhang L, Chen Y, Li Z, Li L, Saint-Cricq P, Li C, Lin J, Wang C, Su Z, Zink JI. Tailored synthesis of octopus-type janus nanoparticles for synergistic actively-targeted and chemo-photothermal therapy. Angew. Chem. Int. Ed. 2016; 55: 2118−2121.

25. Song J, Huang P, Duan H, Chen X. Plasmonic vesicles of amphiphilic nanocrystals: optically active multifunctional platform for cancer diagnosis and therapy. Acc. Chem. Res. 2015; 48: 2506−2515.

26. Song J, Yang X, Jacobson O, Lin L, Huang P, Niu G, Ma Q, Chen X. Sequential drug release and enhanced photothermal and photoacoustic effect of hybrid reduced graphene oxide-loaded ultrasmall gold nanorod vesicles for cancer therapy. ACS Nano, 2015; 9: 9199−9209.

27. Luo G, Chen W, Lei Q, Qiu W, Liu Y, Cheng Y, Zhang XZ. A triple-collaborative strategy for high-performance tumor therapy by multifunctional mesoporous silica-coated gold nanorods. Adv. Funct. Mater. 2016; 26: 4339−4350.

28. Yin W, Yan L, Yu J, Tian G, Zhou L, Zheng X, Zhang X, Yong Y, Li J, Gu Z, Zhao Y. High-throughput synthesis of single-layer MoS2 nanosheets as a near-infrared photothermal-triggered drug delivery for effective cancer therapy. ACS Nano, 2014; 8: 6922−6933.

29. Yang G, Gong H, Liu T, Sun X, Cheng L, Liu Z. Two-dimensional magnetic WS2@Fe3O4 nanocomposite with mesoporous silica coating for drug delivery and imaging-guided therapy of cancer. Biomaterials 2015; 60: 62−71.

30. Lu F, Wang J, Yang L, Zhu JJ. A facile one-pot synthesis of colloidal stable, monodisperse, highly PEGylated CuS@mSiO2 nanocomposites for the combination of photothermal therapy and chemotherapy. Chem. Commun. 2015; 51: 9447−9450.

31. Zhou S, Ma D, Zhang S, Wang W, Chen W, Huang S, Yu K. PEGylated Cu3BiS3 hollow nanospheres as a new photothermal agent for 980 nm-laser-driven photothermochemotherapy and a contrast agent for X-ray computed tomography imaging. Nanoscale 2016; 8: 1374−1382.

32. Tian G, Zhang X, Zheng X, Yin W, Ruan L, Liu X, Zhou L, Yan L, Li S, Gu Z, Zhao Y. Multifunctional RbxWO3 nanorods for simultaneous combined chemo-photothermal therapy and photoacoustic/CT imaging. Small 2014; 10: 4160−4170.

33. Bao T, Yin W, Zheng X, Zhang X, Yu J, Dong X, Yong Y, Gao F, Yan L, Gu Z, Zhao Y. One-pot synthesis of PEGylated plasmonic MoO3ex hollow nanospheres for photoacoustic imaging guided chemo-photothermal combinational therapy of cancer. Biomaterials 2016; 76: 11−24.

34. Song X, Wang X, Yu S, Cao J, Li S, Li J, Liu G, Yang H, Chen X. Co9Se8 nanoplates as a new theranostic platform for photoacoustic/magnetic resonance dual-modal-imaging-guided chemo-photothermal combination therapy. Adv. Mater. 2015; 27: 3285−3291.

35. Fang W, Tang S, Liu P, Fang X, Gong J, Zheng N. Pd nanosheet-covered hollow mesoporous silica nanoparticles as a platform for the chemo-photothermal treatment of cancer cells. Small 2012; 8: 3816−3822.

36. Tang S, Chen M, Zheng N. Multifunctional ultrasmall Pd nanosheets for enhanced near-infrared photothermal therapy and chemotherapy of cancer. Nano Res. 2015; 8: 165−174.

37. C Wang, Xu H, Liang C, Liu Y, Li Z, Yang G, Cheng L, Li Y, Liu Z. Iron oxide @ polypyrrole nanoparticles as a multifunctional drug carrier for remotely controlled cancer therapy with synergistic antitumor effect. ACS Nano 2013; 7: 6782−6795.

38. Gong H, Cheng L, Xiang J, Xu H, Feng L, Shi X, Liu Z. Near-infrared absorbing polymeric nanoparticles as a versatile drug carrier for cancer combination therapy. Adv. Funct. Mater. 2013; 23: 6059−6067.

39. Zhang R, Su S, Hu K, Shao L, Deng X, Sheng W, Wu Y. Smart micelle@polydopamine core–shell nanoparticles for highly effective chemo–photothermal combination therapy. Nanoscale 2015; 7: 19722−19731.

40. Liu F, He X, Lei Z, Liu L, Zhang J, You H, Zhang H, Wang Z. Facile preparation of doxorubicin-loaded upconversion@polydopamine nanoplatforms for simultaneous in vivo multimodality imaging and chemophotothermal synergistic therapy, Adv. Healthcare Mater. 2015; 4: 559−568.

41. Wang X, Zhang J, Wang Y, Wang C, Xiao J, Zhang Q, Cheng Y. Multi-responsive photothermal-chemotherapy with drug-loaded melanin-like nanoparticles for synergetic tumor ablation. Biomaterials 2016; 81: 114−124.

42. Lyu Y, Xie C, Chechetka SA, Miyako E, Pu K, Semiconducting Polymer Nanobioconjugates for Targeted Photothermal Activation of Neurons. J. Am. Chem. Soc. 2016; 138: 9049−9052.

43. Sharifi S, Behzadi S, Laurent S, Forrest M. L, Stroeve P, Mahmoudi M. Toxicity of nanomaterials. Chem. Soc. Rev. 2012; 41: 2323−2343.

44. Dong L, Li M, Zhang S, Li J, Shen G, Tu Y, Zhu J, Tao J. Cytotoxicity of BSA-stabilized gold nanoclusters: in vitro and in vivo study. Small 2015; 11: 2571−2581.

45. Ou G, Li Z, Li D, Cheng L, Liu Z, Wu H. Photothermal therapy by using titanium oxide nanoparticles. Nano Res. 2016; 9: 1236−1243.

46. Rengan AK, Bukhari AB, Pradhan A, Malhotra R, Banerjee R, Srivastava R, De A. In vivo analysis of biodegradable liposome gold nanoparticles as efficient agents for photothermal therapy of cancer. Nano Lett. 2015; 15: 842−848.

47. Park JH, Gu L, Maltzahn G, Ruoslahti E, Bhatia SN, Sailor MJ. Biodegradable luminescent porous silicon nanoparticles for in vivo applications. Nat. Mater. 2009; 8: 331−336.

48. Godin B, Chiappini C, Srinivasan S, Alexander JF, Yokoi K, Ferrari M, Decuzzi P, Liu X. Discoidal porous silicon particles: fabrication and biodistribution in breast cancer bearing mice. Adv. Funct. Mater. 2012; 22: 4225−4235.

49. Gu L, Hall DJ, Qin Z, Anglin E, Joo J, Mooney DJ, Howell SB, Sailor MJ. In vivo time-gated fluorescence imaging with biodegradable luminescent porous silicon nanoparticles. Nat. Commun. 2013; 4: 2326.

50. Maher S, Alsawat M, Kumeria T, Fathalla D, Fetih G, Santos A, Habib F, Losic D. Luminescent silicon diatom replicas: self-reporting and degradable drug carriers with biologically derived shape for sustained delivery of therapeutics. Adv. Funct. Mater. 2015; 25: 5107−5116.

51. Alhmoud H, Delalat B, Elnathan R, Cifuentes-Rius A, Chaix A, Rogers ML, Durand JO, Voelcker NH. Porous silicon nanodiscs for targeted drug delivery. Adv. Funct. Mater. 2015; 25: 1137−1145.

52. Shrestha N, Araújo F, Shahbazi M, Mäkilä E, João Gomes M, Herranz-Blanco B, Lindgren R, Granroth S, Kukk E, Salonen J, Hirvonen J, Sarmento B, Santos HA. Thiolation and Cell-penetrating peptide surface functionalization of porous silicon nanoparticles for oral delivery of insulin. Adv. Funct. Mater. 2016; 26: 3405−3416.

53. Wang Y, Wang K, Zhang R, Liu X, Yan X, Wang J, Wagner E, Huang R. Synthesis of core-shell graphitic carbon@silica nanospheres with dual-ordered mesopores for cancer-targeted photothermochemotherapy. ACS Nano 2014; 8: 7870−7879.

54. Wang H, Sun Y, Yi J, Fu J, Di J, Alonso AC, Zhou S. Fluorescent porous carbon nanocapsules for two-photon imaging, NIR/pH dual-responsive drug carrier, and photothermal therapy. Biomaterials 2015; 53: 117−126.

55. Zhou M, Liu S, Jiang Y, Ma H, Shi M, Wang Q, Zhong W, Liao W, Xing MMQ. Doxorubicin-loaded single wall nanotube thermo-sensitive hydrogel for gastric cancer chemo-photothermal therapy. Adv. Funct. Mater. 2015; 25: 4730−4739.

56. Zhu X, Feng W, Chang J, Tan YW, Li J, Chen M, Sun Y, Li F. Temperature-feedback upconversion nanocomposite for accurate photothermal therapy at facile temperature. Nat. Commun. 2016; 7: 10437.

57. Li W, Li Z, Kang W, Tang Y, Zhang Z, Yang X, Xue H, Lee CS. Hollow nanospheres of loosely packed Si/SiOx nanoparticles encapsulated in carbon shells with enhanced performance as lithium ion battery anodes. J. Mater. Chem. A 2014; 2: 12289−12295.

58. Li W, Tang Y, Kang W, Zhang Z, Yang X, Zhu Y, Zhang W, Lee CS. Core-shell Si/C nanospheres embedded in bubble sheet-like carbon film with enhanced performance as lithium ion battery anodes. Small, 2015; 11: 1345−1351.

59. Feng T, Ai X, An G, Yang P, Zhao Y. Charge-convertible carbon dots for imaging-guided drug delivery with enhanced in vivo cancer therapeutic efficiency. ACS Nano 2016; 10: 4410−4420.

60. Zhu J, Liao L, Bian X, Kong J, Yang P, Liu B. pH-controlled delivery of doxorubicin to cancer cells, based on small mesoporous carbon nanospheres. Small 2012; 8: 2715−2720.

61. Peng F, Su Y, Wei X, Lu Y, Zhou Y, Zhong Y, Lee ST, He Y. Silicon-nanowire-based nanocarriers with ultrahigh drug-loading capacity for in vitro and in vivo cancer therapy. Angew. Chem. Int. Ed. 2013; 52: 1457−1461.

62. Feng L, Li K, Shi X, Gao M, Liu J, Liu Z. Smart pH-responsive nanocarriers based on nano-graphene oxide for combined chemo- and photothermal therapy overcoming drug resistance. Adv. Healthcare Mater. 2014; 3: 1261−1271.

63. Yang G, Gong H, Qian X, Tan P, Li Z, Liu T, Liu J, Li Y, Liu Z. Mesoporous silica nanorods intrinsically doped with photosensitizers as a multifunctional drug carrier for combination therapy of cancer. Nano Res. 2015; 8: 751−764.

64. Hessel CM, Pattani VP, Rasch M, Panthani MG, Koo B, Tunnell JW, Korgel BA. Copper selenide nanocrystals for photothermal therapy. Nano Lett. 2011; 11: 2560−2566.

65. Wang S, Riedinger A, Li H, Fu C, Liu H, Li L, Liu T, Tan L, Barthel MJ, Pugliese G, Donato FD, D'Abbusco MS, Meng X, Manna L, Meng H, Pellegrino T. Plasmonic copper sulfide nanocrystals exhibiting near-infrared photothermal and photodynamic therapeutic effects. ACS Nano 2015; 9: 1788−1800.

66. Sheng Z, Hu D, Zheng M, Zhao P, Liu H, Gao D, Gong P, Gao G, Zhang P, Ma Y, Cai L. Smart human serum albumin-indocyanine green nanoparticles generated by programmed assembly for dual-modal imaging-guided cancer synergistic phototherapy. ACS Nano, 2014; 8: 12310−12322.

67. Wei W, Zhang X, Chen X, Zhou M, Xu R, Zhang X. Smart surface coating of drug nanoparticles with cross-linkable polyethylene glycol for bio-responsive and highly efficient drug delivery. Nanoscale, 2016; 8: 8118−8125.

68. Zhang J, Li Y, An FF, Zhang X, Chen X, Lee CS. Preparation and size control of sub-100 nm pure nanodrugs. Nano Lett. 2015; 15: 313−318.

69. Wang L, Gao B, Peng C, Peng X, Fu J, Chu PK, Huo K. Bamboo leaf derived ultrafine Si nanoparticles and Si/C nanocomposites for high-performance Li-ion battery anodes. Nanoscale 2015; 7: 13840−13847.

70. Ahn J, Kim H, Pyo J, Lee J, Yoo W, Variation in Crystalline Phases: Controlling the Selectivity between Silicon and Silicon Carbide via Magnesiothermic Reduction using Silica/Carbon Composites. Chem. Mater. 2016; 28: 1526−1536.